## RESEARCH ARTICLE

Check for updates

# A multifunctional organophosphonic ligand-templated poly(polyoxotungstate) with potential in building a genosensor for thalassemia gene detection†

Wenshu Zhang,[b] Zixu Wang,[b] Mengya Cao,[b] Dan Wang,*[a,b] Lijuan Chen*[b] and Junwei Zhao [ID] *[b]

A novel $P^V$–$Sb^{III}$ heteroatom-inserted poly(polyoxotungstate) (poly(POT)) $[H_2N(CH_3)_2]_5Na_{11}H_9[(HEDATMPA)$ $SbW_{15}O_{50}]\{[PrW_4O_{10}][B\text{-}\alpha\text{-}SbW_9O_{33}]_2\}\cdot38H_2O$ (**1**) was synthesized and is composed of an attractive $[(HEDATMPA)SbW_{15}O_{50}]^{14-}$ hybrid fragment and one sandwich-like $Pr^{III}$-inserted $[PrW_4O_{10}(B\text{-}\alpha\text{-}SbW_9O_{33})_2]^{11-}$ entity by using ethylenediamine tetramethylphosphoric acid ($H_8EDATMPA$) with potential heteroatom sites and functional organic groups. Considering the advantages of poly(POT) clusters in storing and transferring electrons, we fabricated a **1**-PEDOT (PEDOT = poly(3,4-ethylenedioxythiophene)) hybrid film, which was used as an electrode-modified material to construct a **1**-based genosensor (GS) for detecting the β-thalassemia gene. Research results show that this **1**-based GS demonstrates high specificity, outstanding antijamming ability and low detection limit for β-thalassemia gene detection. This work not only provides a novel and feasible preparative strategy to construct poly(POT) clusters, but also promisingly promotes the development of poly(POT)-based GSs.

## Introduction

Metal–oxygen clusters have been widely acknowledged as star candidates in diverse fields (*e.g.* catalysis, energy storage, biomedicine and photoelectric materials), which mainly benefits from their abundant structures, skeleton size and functional components.[1–3] Among metal–oxygen cluster materials, polyoxotungstates (POTs), mainly formed from tungsten centers and oxygen linkers, have been extensively studied since more and more applications of POTs are being discovered in different fields.[4–8]

It is worth mentioning that the introduction of heteroatoms (HAs) in the tungsten-oxo reaction system can produce lacunary POT units.[7,9] It has been revealed that due to abundant surface reactive oxygen sites, lacunary POT units can work as rigid multidentate inorganic ligands to coordinate with func-

tional components such as rare-earth (RE) ions, transition-metal (TM) ions and organic ligands.[10] Because of diverse coordination sites and flexible combination modes between POT units and functional components, a great deal of attractive poly(POT) clusters have been obtained.[11–13] Particularly, organic–inorganic hybrid POTs have been considered as one important branch in POT chemistry because various organic ligands can provide a great opportunity for creating novel poly (POT) hybrids.[8,14,15] For example, with the assistance of fumaric acid, our group prepared a fascinating RE-encapsulated poly(POT) hybrid $\{[RE_3(H_2O)_7]_2[W_4O_8(C_4H_2O_4)(C_4H_3O_4)]_2$ $[SeW_6O_{25}]_2[B\text{-}\alpha\text{-}SeW_9O_{33}]_4\}^{24-}$ (RE = $Ce^{3+}$, $La^{3+}$, Fig. S1a†), in which two fumaric acid ligands bridge two $\{[RE_3(H_2O)_7]$ $[W_4O_8(C_4H_2O_4)(C_4H_3O_4)][SeW_6O_{25}][B\text{-}\alpha\text{-}SeW_9O_{33}]_2\}^{12-}$ moieties.[15] In 2019, Ding and his colleagues utilized citric acid ($H_4CIT$) as the organic ligand and isolated a strip-shaped octamer $[Eu_{16}Co_7Se_{16}W_{128}O_{448}(CIT)_{10}$ $(HCIT)_2(NO_3)_4(OH)_4(H_2O)_{52}]^{48-}$ (Fig. S1b†), which represents the longest poly(POT) macro-molecule at that time.[13] This macromolecule consists of two tetrameric $\{Eu_8Se_8W_{64}Co_3O_{224}(OH)_2(NO_3)_2(CIT)_6(H_2O)_{26}\}$ segments joined together by $H_4CIT$ ligands and TM ions. It is to be noted that not only the introduction of organic ligands tremendously makes for the formation of poly(POT) hybrids, but also the addition of RE ions helps in gathering adjacent POT units together.[6,16]

*[a]School of Pharmacy and Henan Province Engineering Research Center of High Value Utilization to Natural Medical Resource in Yellow River Basin, Henan University, Kaifeng 475004, China. E-mail: wangdan@henu.edu.cn*
*[b]Henan Key Laboratory of Polyoxometalate Chemistry, College of Chemistry and Molecular Sciences, Henan University, Kaifeng, Henan 475004, China. E-mail: ljchen@henu.edu.cn, zhaojunwei@henu.edu.cn*

Until now, although many innovative poly(POT) hybrids have been greatly developed, oriented design and precise synthesis of poly(POT) clusters remain a challenge. It has been found that POT precursors, HAs or organic ligands can function as the template-guiding role in the formation of poly(POT) clusters.[17–19] The well-defined template can effectively induce the assembly of multiple components. HAs have been often used as the template-guiding agent to induce the aggregation of POT units. For instance, by employing $SeO_3^{2-}$ as the template, Cronin's group acquired a battery of high-nuclear POTs $[H_2(SeO_3)_3W_{43}O_{139}]^{24-}$, $[H_4(SeO_3)_5W_{77}O_{250}]^{44-}$, $[H_6(SeO_3)_6W_{63}O_{203}]^{34-}$ and $[H_8(SeO_3)_{16}W_{101}O_{317}]^{52-}$ (Fig. 1a), highlighting that the HA template ($SeO_3^{2-}$) effectively can give rise to lacunary $\{SeW_9O_{33}\}$ units instead of the "closed" saturated Keggin-type $\{SeW_{12}O_{40}\}$ cluster.[20] In recent years, researchers have no longer been satisfied with the studies of single HA-inserted POTs and have begun to introduce different types of HAs into a one POT system. Cronin's group and Zhao's group have demonstrated the feasibility of using dual-HA templates to synthesize novel poly(POT) clusters with novel layered POT building blocks $\{XX'W_{15}O_{54}\}$ (X = HP[III], Bi[III], X' = Se[III], Te[VI], As[III], Sb[III]), providing a promising approach for continually discovering POT architectures (Fig. 1b–d).[19,21–23] Beyond that, the critical template-guiding role of organic ligands can't be ignored. A typical example is the group of multi-Ni[II] substituted silicotungstate clusters $\{SiW_9Ni_4\}_{2n}L_{3n}$ (n = 2, 3); $\{SiW_9Ni_4\}$ = ([(A-α-SiW_9O_{34})Ni_4(OH)_3]^{5-}, L = ligand) with regulable interior voids (Fig. 1e).[24] In this work, by utilizing the $[A-α-SiW_9O_{34}]^{10-}$ precursors as inorganic nodes and rigid ligands with different bending angles as linkers, Fang *et al.* successfully realized the regulation of the skeletons and interior voids of $\{SiW_9Ni_4\}_{2n}L_{3n}$.[24]

In previous research studies, it has been proved that some elemento-organic compounds can be used as template linkers or provide HA templates to construct uncommon poly(POT) hybrids.[6,14,25] As early as in 2000, Pope's group introduced phenyltin trichloride (PhSn)Cl$_3$ into the POT system and obtained sandwich-like POT clusters $[(PhSn)_3Na_3(α-SbW_9O_{33})_2]^{6-}$ and $[\{(PhSn)_2O\}_2H(α-AsW_9O_{33})_2]^{9-}$, in which organotin ligands serve as a template linker to join two $[α-XW_9O_{33}]^{9-}$ (X = Sb[III] and As[III]) building blocks (Fig. 1f).[26] In 2020, organoboronic ligands (BBLs) were first introduced into the POT system and led to tetrameric $[\{BBL\}_4(M_3P_2W_{15}O_{62})_4]^{28-}$ and dodecameric $[\{BBL\}_{15}(M_3P_2W_{15}O_{62})_{12}]^{86-}$ (M = Ta[V], Nb[V]), in which each BBL covalently links to three Dawson-like lacunary POT blocks (Fig. 1g).[27] More interestingly, in the organophosphonic ligand modified poly(POT) cluster $\{[(AsW_9O_{33})Zn(H_2O)W_5O_{13}(N(CH_2PO_3)_3)]_2\}^{14-}$, aminotrimethylene phosphonic ligands serve as the HA-supplier other than the organic linker (Fig. 1h).[28] Based on these results, given that both HAs and organic ligands can simultaneously act as templates for the assembly of poly(POT) clusters, it is possible that special organic ligands containing both potential HA sites and functional coordination groups will play a dual-template-guiding role. That is to say, these special organic ligands not only work as template linkers to combine with POT different blocks, but also can provide HA templates to induce novel building blocks. Thus, we began to use elemento-organic ligands with potential HA sites and functional organic groups to react with the POT precursors in the participation of RE ions for searching for innovative poly(POT) clusters.

In this work, we chose ethylenediamine tetramethylphosphonic acid (H$_8$EDATMPA) (Fig. S2†) with potential HA sites and functional organic groups as the multifunctional ligand and successfully obtained a P[V]–Sb[III] double-HA intercalated poly(POT) cluster $[H_2N(CH_3)_2]_5Na_{11}H_9$ $[(HEDATMPA)SbW_{15}O_{50}]\{[PrW_4O_{10}][B-α-SbW_9O_{33}]_2\}·38H_2O$ (**1**). In the polya-
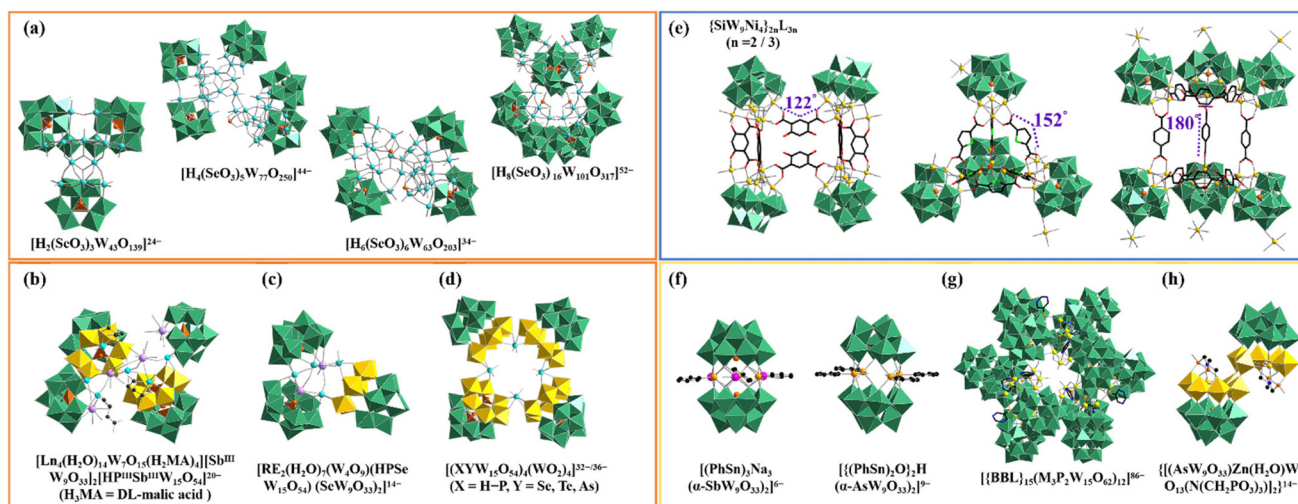


**Fig. 1** (a) Some poly(POT) clusters using single-HA templates. (b–d) Some poly(POT) clusters with double-HA templates. (e) Some organic ligands regulated poly(POT) clusters. (f) Two poly(POT) clusters based on organotin linkers. (g) An organoboronic ligand-modified poly(POT) cluster. (h) A organophosphonic modified poly(POT) cluster ($\{WO_6\}$: green and yellow octahedra).

This journal is © the Partner Organisations 2024

*Inorg. Chem. Front.*, 2024, **11**, 602–612 | **603**

nion of **1**, as expected, HEDATMPA[7−] not only offers the P[V] center as the HA template contributing to a layered [(HEDATMPA)SbW$_{15}$O$_{50}$][14−] building block, but also works as a linker to bridge [(HEDATMPA)SbW$_{15}$O$_{50}$][14−] and {PrW$_4$O$_{10}$[B-α-SbW$_9$O$_{33}$]$_2$}[11−] entities. Moreover, **1** was composited with poly(3,4-ethylenedioxythiophene) (PEDOT) to prepare the **1**-PEDOT hybrid film using the electropolymerization strategy. Furthermore, the **1**-PEDOT film was utilized as the electrode-modified material to construct the **1**-based genosensor (GS) for the β-thalassemia gene detection. The constructed **1**-based GS shows high sensitivity as well as strong anti-interference ability in determining the β-thalassemia gene. Undoubtedly, this work provides a new idea for the design and synthesis of novel poly(POT) aggregates and enriches the application of poly(POT)-based materials in the detection of genes.

## Results and discussion

### Structure description

The agreement of experimental and simulated powder X-ray diffraction curves of **1** indicates the good phase purity of the collected crystals (Fig. S3†). Subsequently, IR spectroscopy (Fig. S4†) and thermogravimetric analysis (Fig. S5†) were conducted to characterize **1**. The crystallographic data (Table S1†) show that **1** belongs to the $P\bar{1}$ space group. The polyanion [[(HEDATMPA)SbW$_{15}$O$_{50}$]{[PrW$_4$O$_{10}$[B-α-SbW$_9$O$_{33}$]$_2$]}][25−] (**1a**) features an HEDATMPA[7−] connecting trimeric hybrid architecture (Fig. 2a). Specifically, **1a** can be deemed as an aggregate of a Dawson-like [(HEDATMPA) SbW$_{15}$O$_{50}$][14−] entity and a sandwich-like Pr[III]-inserted {PrW$_4$O$_{10}$[B-α-SbW$_9$O$_{33}$]$_2$}[11−] segment bridged by a HEDATMPA[7−] linker (Fig. 2b). It should be highlighted that the organic–inorganic hybrid Dawson-like [(HEDATMPA)SbW$_{15}$O$_{50}$][14−] entity can be imagined as a second HA (P[V]) embedded [(HEDATMPA)W$_6$O$_{27}$][25−] subunit grafting onto a trivacant Keggin [B-α-SbW$_9$O$_{33}$][9−] fragment (Fig. 2c). More significantly, the P[V] HA comes from the organophosphonic ligand. In other words, due to the template-guiding effect of the P[V]1 atom in the organophosphonic ligand, six {WO$_6$} octahedra were successfully induced to form a {C$_6$N$_2$P$_4$W$_6$} ring around the P[V]1 HA, and further connect the {Sb1W$_9$} block by sharing apical oxygen atoms. Meanwhile, another phosphate group in the organophosphonic ligand provides the P[V]2 atom to share an oxygen atom with the W13 atom, leading to a chelate ring, which will potentially stabilize the skeleton (Fig. 2d). More than being an HA provider, the organophosphonic ligand also functions as the linker between adjacent POT fragments. To be specific, the left two phosphate groups on the other side of the organophosphonic ligand further joined two [W$_2$O$_{11}$][10−] units to form the [(POCH$_2$O$_2$)$_3$(POCH$_3$O$_2$)C$_2$H$_4$N$_2$W$_4$O$_{18}$][19−] {C$_6$N$_2$P$_4$W$_4$} segment (Fig. 2e and f), which is encapsulated by the [PrO$_4$(B-α-SbW$_9$O$_{33}$)$_2$][23−] ({PrSb$_2$W$_{18}$}) entity. As for the sandwich-like {PrSb$_2$W$_{18}$} unit (Fig. 2g), it can be observed that the eight-coordinated Pr1[3+] ion adopts a distorted bicapped triangular prismatic geometry and connects two {SbW$_9$} subunits
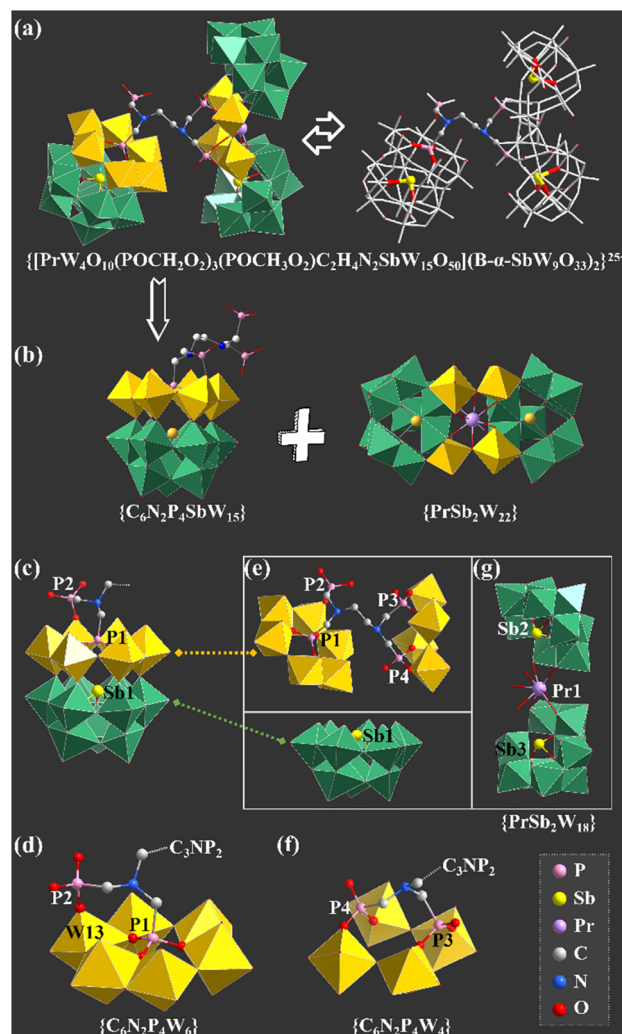


**Fig. 2** (a) The **1a** polyanion. (b) The Dawson-like [(HEDATMPA) SbW$_{15}$O$_{50}$][14−] entity and the sandwich-type {PrW$_4$O$_{10}$[B-α-SbW$_{33}$)$_2$][11−] segment. (c) The Dawson-like [(HEDATMPA) SbW$_{15}$O$_{50}$][14−] entity. (d) The {C$_6$N$_2$P$_4$W$_6$} ring with the P1[V] atom as the HA. (e) The bridging role of the organophosphonic ligand. (f) The {C$_6$N$_2$P$_4$W$_4$} segment. (g) The sandwich-like {PrSb$_2$W$_{18}$} unit.

through Pr–O–W bonds (Fig. S6 and S7†). Interestingly, in the whole structure, four P[V] atoms in the organophosphonic ligand exhibit three different coordination modes. Three oxygen atoms in the –P1O$_3$H$_2$ group are all coordinated with W atoms, while the P2 atom has two uncoordinated oxygen atoms (Fig. S7a and b†). On the other side of the ligand, both P3 and P4 atoms provide two oxygen atoms to connect additional W atoms (Fig. S7c and d†).

So as to demonstrate the structural novelty of **1**, the polyanion **1a** is here compared with the reported selenotungstate anion [Ce$_2$(H$_2$O)$_7$(W$_4$O$_9$) (HP[III]SeW$_{15}$O$_{54}$)(SeW$_9$O$_{33}$)$_2$][14−] (**2a**), which is similar to **1a** and contains a pure inorganic Dawson-like [HP[III]SeW$_{15}$O$_{54}$][11−] ({HP[III]SeW$_{15}$}) fragment (Fig. 3a).[22] This {HP[III]SeW$_{15}$} entity in **2a** consists of a firstly reported [HP[III]W$_6$O$_{27}$][14−] ({HP[III]W$_6$}) subunit with P[III] as the second HA

**604** | *Inorg. Chem. Front.*, 2024, **11**, 602–612
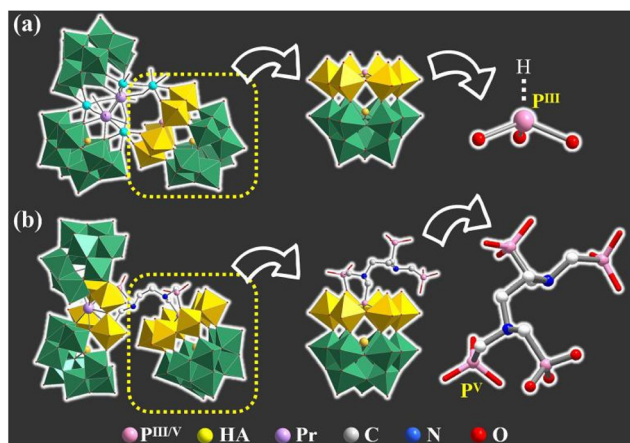
This journal is © the Partner Organisations 2024

**Fig. 3** Comparison of the inorganic HP$^{III}$-inserted Dawson-like {HP$^{III}$SeW$_{15}$} unit in **2a** (a) and the organic–inorganic hybrid {C$_6$N$_2$P$_4$SbW$_{15}$} unit in **1a** (b).

located on the top of the classical {SeW$_9$} fragment. As we know, the coordination number of the P$^{III}$ atom from inorganic phosphorous acid is four. Thus, the P$^{III}$ atom in the {HP$^{III}$SeW$_{15}$} entity can't further coordinate with other functional components such as organic ligands or metal ions. Therefore, structural expansion of the {HP$^{III}$SeW$_{15}$} entity can be only achieved through the active oxygen sites in the {WO$_6$} octahedra. In comparison, the {C$_6$N$_2$P$_4^V$SbW$_{15}$} block with the P$^V$ atoms from the organophosphonic ligand in **1a** has exposed oxygen sites from tungsten–oxygen clusters and coordination-active oxygen sites from organic groups, which offers more opportunity to bridge more POT blocks together (Fig. 3b). This result indicates that such organophosphonic ligand is supposed to provide more chances for achieving novel poly(POT) aggregates.

In the crystal structure, some lattice water molecules, [H$_2$N(CH$_3$)$_2$]$^+$, Na$^+$ and H$^+$ cations can interact with **1a** polyanions through hydrogen bonding interactions and electrostatic attraction.[29] Moreover, **1a** polyanions, counter cations and lattice water molecules are arranged orderly in three axes. In order to more clearly describe the three-dimensional stacking mode of **1a** polyanions, we omit those charge compensation ions here and further leave only Sb1, Sb2 and Sb3 atoms in the structure, simplifying the **1a** polyanion into a triangle. It is clearly observed that the **1a** polyanions exhibit an "–ABAB–" stacking pattern along the $a$, $b$, and $c$ axes, respectively (Fig. S8†).
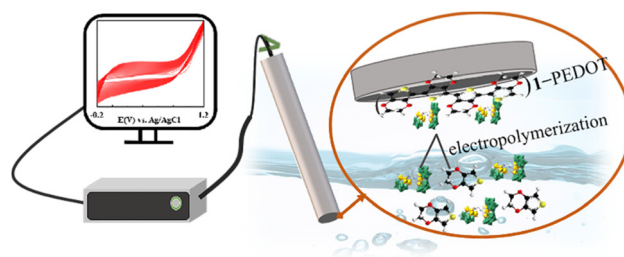
**Characterization of the 1-based hybrid film**

Recently, the electrochemistry of poly(POT) clusters has been explosively studied, especially in electrochemical catalysts/sensors, energy-related devices and so on.[8,21,30] Owing to their reversible electron transmittability between stable skeletons, poly(POT) clusters have been considered as promising candidates in electrochemical applications.[31] Except that they can

be used as electron conductors, poly(POT) clusters have also been demonstrated to be stability-enhancers, conductivity-facilitators, or even electronic repositories.[32–34] Nevertheless, the advancements of poly(POT) clusters in electrochemistry have been limited by their water-solubility. To break this bottleneck, more and more preparative methods for poly(POT)-based composite materials have been put forward, for instance, physical adsorption,[21] chemical/electro-deposition,[35] layer-by-layer assembly,[36] and electropolymerization.[37] As the electropolymerization technology can provide uniform polymeric films with high chemical/electrochemical stability and remarkable conductivity, it has become a favored route to modify electrodes in constructing electrochemical sensors or devices.[38] It is well-known that PEDOT has been widely used as a conductive polymer, which was first reported in the early 1990s, and has characteristics of excellent conductivity, good film-forming performance and a long cycle life.[39,40] Herein, we successfully prepared a hybrid film **1**-PEDOT *via* an electropolymerization process in the mixed solution of **1** and 3,4-ethylenedioxythiophene (EDOT). Therefore, the prepared **1**-PEDOT hybrid film was also supposed to show outstanding electrochemical properties.

The homogeneous **1**-PEDOT film was constructed based on a typical three-electrode platform, including a glassy carbon electrode (GCE) as the working electrode, an auxiliary platinum electrode, and the reference silver electrode. As shown in Scheme 1, the electropolymerization process was realized through a cyclic voltammetry (CV) method under −0.2–1.2 V potential in a mixed solution containing **1**, EDOT and NaClO$_4$. During the electropolymerization, **1a** polyanions and protonated EDOT migrate to the surface of GCE under the electric field. The polymerization results in a uniform **1**-PEDOT film firmly attached to the GCE surface.

Since the reaction took place in aqueous solution, the stability of **1** in water was first tested by electrospray ionization mass spectrometry (ESI-MS). In the ESI-MS spectrum, three obvious ESI-MS signals at $m/z$ 1424.22 (7−), 1665.31 (6−) and 2012.26 (5−) were observed and can be respectively assigned to {Na$_9$H$_9$[PrW$_4$O$_{10}$(POCH$_2$O$_2$)$_3$(POCH$_3$O$_2$)C$_2$H$_4$N$_2$SbW$_{15}$O$_{50}$][B-α-SbW$_9$O$_{33}$]$_2$}$^{7-}$, {Na$_{10}$H$_9$[PrW$_4$O$_{10}$(POCH$_2$O$_2$)$_3$(POCH$_3$O$_2$)C$_2$H$_4$N$_2$SbW$_{15}$O$_{50}$][B-α-SbW$_{933}$]$_2$}$^{6-}$ and {[H$_2$N(CH$_3$)$_2$]Na$_9$H$_9$[PrW$_4$O$_{10}$(POCH$_2$O$_2$)$_3$(POCH$_3$O$_2$)C$_2$H$_4$N$_2$SbW$_{15}$O$_{50}$][B-α-SbW$_9$



**Scheme 1** Schematic diagram of preparing the **1**-PEDOT modified electrode.

This journal is © the Partner Organisations 2024

*Inorg. Chem. Front.*, 2024, **11**, 602–612 | **605**

$O_{33}]_2\}^{5-}$ segments, which implies that the basic skeleton of the **1a** polyanion is stable in aqueous solution (Fig. S9†). Moreover, we monitored the structure variation of the **1a** polyanion after dissolving it in an aqueous solution for different times by ultraviolet–visible (UV–vis) absorption spectroscopy. As the UV–vis spectra of **1** in the aqueous solution almost remained constant over time (Fig. S10†), the stability of the **1a** polyanion in water is demonstrated, laying the foundation for its further application exploration.

Besides, in order to confirm the successful preparation of the **1**-based film, CV curves of the naked electrode and different modified electrodes were collected using a 0.2 mol $L^{-1}$ $CH_3COOH$–$CH_3COONa$ buffer solution (pH = 4.5, Fig. 4a). It can be observed that there are no paired redox peaks of PEDOT in the $CH_3COOH$–$CH_3COONa$ buffer solution, while a couple of redox peaks can be observed in the CV curve of **1**-PEDOT after electropolymerization, which may imply the successful recombination of **1** and PEDOT. To further verify the combination of **1** and PEDOT in the hybrid film, IR spectra (Fig. S11†), X-ray photoelectron spectroscopy (XPS, Fig. 4b and Fig. S12, S13†) and energy dispersive spectroscopy (EDS) elemental mapping (Fig. S14†) measurements of **1**, PEDOT and the **1**-PEDOT film were carried out. It can be seen from the comparison of IR spectra of **1**, PEDOT and the **1**-PEDOT film (Fig. S11†) that the characteristic bands of both **1** [1065 ($P^V$–O), 948 (W–$O_t$), 899 (W–$O_b$), 780 (W–$O_c$) and 718 $cm^{-1}$ ($Sb^{III}$–$O_a$)] and PEDOT [1521 $cm^{-1}$ (C=C), 686 $cm^{-1}$ (C–S)][40] can be observed in the IR spectrum of **1**-PEDOT, stating the co-existence of **1** and PEDOT in the **1**-PEDOT film. In the mean-

time, comparing the XPS spectrum of **1** and that of the **1**-PEDOT film, we can see that both the characteristic peaks of **1** (W $4f_{7/2}$: 35.9 eV, W $4f_{5/2}$: 38.0 eV) and those corresponding to PEDOT (S $2p_{3/2}$: 163.4 eV, S $2p_{1/2}$: 164.6 eV) appear simultaneously in the XPS pattern of the **1**-PEDOT film (Fig. 4c and Fig. S12, S13†).[30,41,42] Furthermore, the EDS mapping images exhibit the uniform distribution of W, P, Sb, Pr and S elements in the **1**-PEDOT film (Fig. S14†). All the above results synthetically evidence the combination of **1** and PEDOT in the **1**-PEDOT hybrid film.

It is well known that electrical conductivity is the primary criterion to determine whether the **1**-PEDOT hybrid film can be used as the electrode modification material. So, experimental conditions for preparing the **1**-PEDOT film as well as follow-up measurements were optimized by taking electrical conductivity (through CV and DPV signals) as the evaluation index. First of all, the electropolymerization cycles that mainly affect the conductivity of the **1**-PEDOT film were optimized by varying the number of sweep cycles (10, 20, 30, 40, 50 and 60 cycles) in the CV preparation procedure. The **1**-PEDOT modified GCE (**1**-PEDOT/GCE) was used as the working electrode and the corresponding CV and DPV curves were collected in 0.10 mol $L^{-1}$ phosphate buffered saline (PBS, pH = 7.4) containing 0.01 mol $L^{-1}$ 1 : 1 $[Fe(CN)_6]^{3-/4-}$ (marked as Fe-PBS). As shown in Fig. S15,† various redox peaks appear under different electropolymerization cycles, which are caused by the faster electron transfer rate on the PEDOT-modified GCE. This performance improvement can be attributed to the larger effective surface area of **1**-PEDOT/GCE.[43] The electroactive area
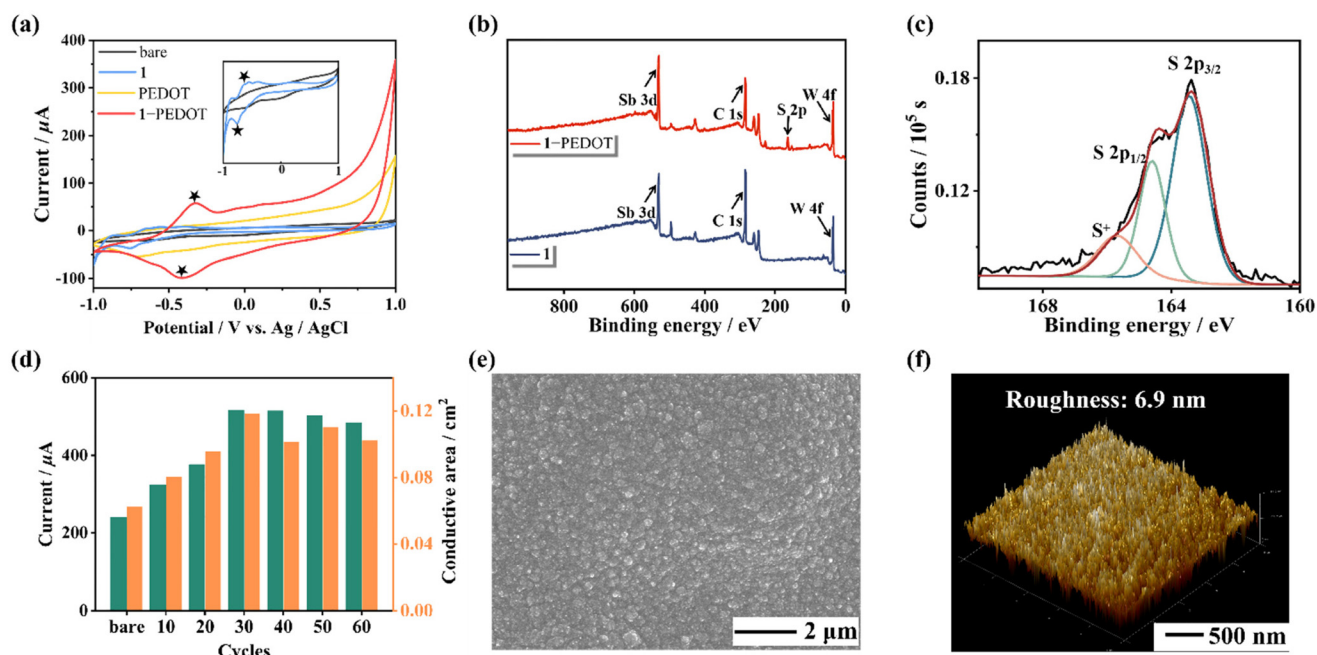


**Fig. 4** (a) CV curves of bare GCE and GCEs modified using **1**, **1**-PEDOT and PEDOT in 0.2 mol $L^{-1}$ $CH_3COOH$–$CH_3COONa$ buffer solution. Inset: CV curves of bare GCE and **1**-PEDOT/GCE. (b) Comparison of XPS spectra between **1** and the **1**-PEDOT film. (c) XPS spectra of S 2p in the **1**-PEDOT film. (d) Comparison of the conductive area and DPV peak of **1**-PEDOT/GCEs with different electropolymerization cycles (0/10/20/30/40/50/60) in the Fe-PBS solution (pH = 7.4). (e and f) SEM and AFM images of the **1**-PEDOT film on the ITO substrate (30 electropolymerization cycles).

**606** | *Inorg. Chem. Front.*, 2024, **11**, 602–612

This journal is © the Partner Organisations 2024

under different sweep cycles in the CV method was calculated according to the Randles–Sevcik equation shown below:

$$I_p = 2.69 \times 10^5 n^{3/2} A D^{1/2} v^{1/2} c$$

Here, $I_p$ refers to the redox peak of the CV curve measured in Fe-PBS (pH = 7.4) solution, $A$ (cm$^2$) is the electrode conductive area, $n$ is the number of transferred electrons ($n$ = 1), $D$ represents the diffusion coefficient of $K_3[Fe(CN)_6]$ ($D$ = 7.6 × 10$^{-6}$ cm$^2$ s$^{-1}$), $v$ represents the scanning rate ($v$ = 0.1 V s$^{-1}$) and $c$ is the concentration of $K_3[Fe(CN)_6]$ ($c$ = 0.01 mol L$^{-1}$).[31] While compared with the bare GCE ($A$ = 0.06 cm$^2$), the modified 1-PEDOT/GCE exhibits a larger electrode conductive area ($A$ = 0.12 cm$^2$), which might be explained by the fact that the 1-PEDOT hybrid film on the GCE surface can provide more exposed redox sites after electropolymerization.[31] It can be seen that on increasing the electropolymerization cycles, the conductive area and the intensity of the DPV current at 0.252 V (Fig. 4d and Fig. S15, S16†) also increase and reach the maximum when the electropolymerization cycle is 30. In other words, the optimized electropolymerization cycle for preparing the 1-PEDOT film is 30. Moreover, it is found from both CV and DPV measurements (Fig. S17†) that the signal strength of CV and DPV peaks and the integral area of the CV curve (that is the electrode conductive area $A$) of 1-PEDOT/GCE are obviously enhanced compared with those of bare GCE, which indicates that the 1-PEDOT film has good electrical conductivity. In order to investigate the influence of the pH value of phosphate buffered saline (PBS) solution on the sensitivity of 1-PEDOT/GCE, a series of 0.10 mol L$^{-1}$ PBS solutions containing 0.01 mol L$^{-1}$ 1 : 1 $[Fe(CN)_6]^{3-/4-}$ with different pH values (pH = 5.4/6.4/7.4/8.4/9.4) were prepared. Then, the DPV curves of 1-PEDOT/GCE were tested in these solutions (Fig. S18†). It can be observed that the detected DPV signal of 1-PEDOT/GCE is the strongest when the pH value is 7.4. Therefore, 7.4 was selected as the optimized pH value and the subsequent experiments were carried out in the pH = 7.4 Fe-PBS solution. At the same time, the electrochemical double-layer capacitance ($C_{dl}$) test is an important method for obtaining the electrochemically active surface area (ECSA) involved in the electrochemical reaction, which can be achieved from CV curves with different scan rates under voltages in the non-Faraday interval.[44,45] Therefore, the modified GCEs were tested by CV technology with different scanning rates (0.02–0.20 V s$^{-1}$) in the voltage range of 0.32–0.42 V. Thus, the $C_{dl}$ of 1-PEDOT/GCE was calculated as 16.56 mF cm$^{-2}$ while that of PEDOT/GCE was calculated as 9.30 mF cm$^{-2}$, indicating the larger ECSA of 1-PEDOT/GCE. That is to say, the participation of 1 significantly improves the ECSA of the film-modified GCE (Fig. S19†).

Subsequently, to investigate the morphology of the 1-PEDOT hybrid film, the 1-PEDOT film was fabricated on the indium-tin oxide (ITO) substrate under optimized conditions and was characterized by scanning electron microscopy (SEM) and atomic force microscopy (AFM). The SEM image clearly demonstrates that the obtained 1-PEDOT film features outstanding flatness and uniformity (Fig. 4e). The AFM image

indicates that the roughness of the 1-PEDOT film is about 6.9 nm (Fig. 4f).

Long-term stability is another critical evaluation criterion for further practical application as electrode materials, so the stability evaluation of the 1-PEDOT hybrid film was conducted. Specifically, the conductivity variation of bare GCEs and 1-PEDOT/GCEs during the natural storage at room temperature for a period of time was monitored by recording their DPV curves. As illustrated in Fig. S20,† the DPV signal intensity of 1-PEDOT/GCE goes down slightly during the storage for 30 days while the bare GCE is fast passivated and the conductivity decreases significantly in two hours. Thus, the 1-PEDOT hybrid film shows good stability, enabling it to be a promising electrode modification material.

### Fabrication of the 1-based GS for β-thalassemia gene detection

Thalassemia is a common genetic defect disease that is chronic hemolytic anemia caused by a disorder of globin peptide chain synthesis, and has been a serious threat to human health.[46] Thus, the growing demand for simple, fast and inexpensive testing measures, as opposed to time-consuming and expensive detection of nucleic acids with specific sequences, has largely encouraged researchers to study GSs for the detection of the thalassemia gene. Until now, diverse response signals (e.g. electrochemistry,[47,48] fluorescence,[49] surface plasmon resonance optics[50]) have been applied in thalassemia GSs. Among them, electrochemical detection has attracted wide attention due to its advantages of low cost, high sensitivity and fast response.

The electrochemical detection of genes usually requires effective modification of the electrode surface to access enhanced signals along with improved stability of the working electrode. Herein, considering that the 1-PEDOT film has good conductivity and stability, we designed a novel GS using the 1-PEDOT/GCE as the working electrode for electrochemical identification of the β-thalassemia gene. The basic principle of this GS is presented in Scheme 2. Firstly, to provide fixed sites for the pDNA chains, Au nanoparticles (NPs) are electrochemically deposited on the surface of 1-PEDOT/GCE (Scheme 2a) through an electrodeposition procedure in AuCl$_4^-$ (0.10 g L$^{-1}$) solution, leading to the Au NP modified electrode (Au/1-PEDOT/GCE, Scheme 2b). Then, 5 μL of a solution containing a sulfhydryl-modified pDAN fragment at one end (5′-SH-ACTTCAGGATG AGTCTATGG-3′) as pDNA is dropped down onto the Au/1-PEDOT/GCE surface to acquire the pDNA graft on the exposed Au sites via Au–S bonds, leading to pDNA/Au/1-PEDOT/GCE (Scheme 2c). Afterwards, the unoccupied Au sites on the electrode surface are closed using 20 μL of 2.0 wt% bovine albumin (BSA) solution to avoid the possible nonspecific adsorption of DNA chains in the subsequent steps (Scheme 2d). Next, 10 μL antisense DNA strand of the human β-thalassemia gene (5′-CCATAGACTCATCCTGAAGT-3′) as the target DNA (tDNA) was dropped onto the surface of BSA-treated pDNA/Au/1-PEDOT/GCE (1-based GS). After a period of time for hybridization, pDNA will capture the tDNA strand forming double helix DNA (dhDNA) on the electrode (marked

This journal is © the Partner Organisations 2024

Inorg. Chem. Front., 2024, 11, 602–612 | 607
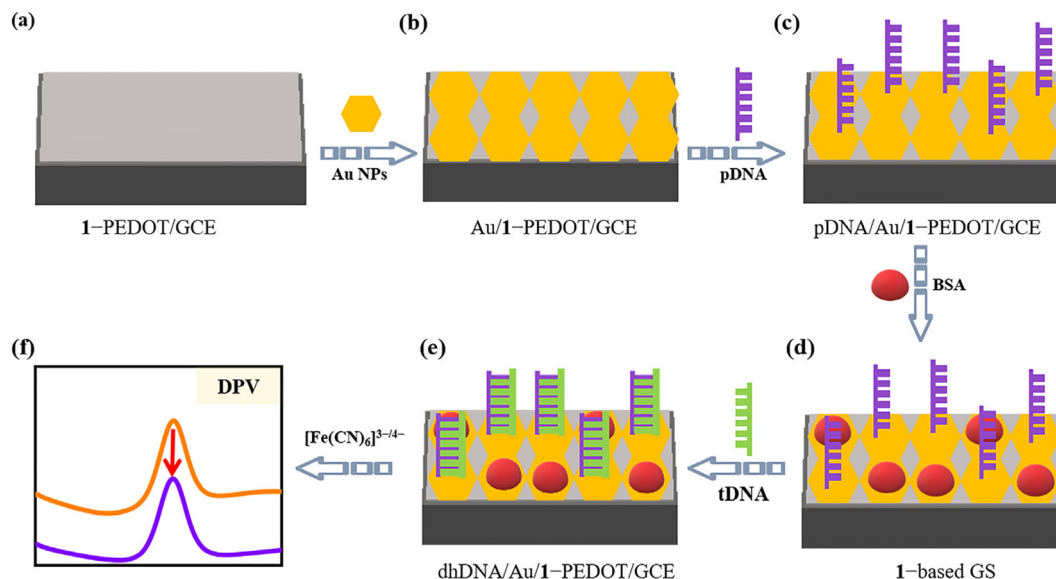
**Scheme 2** Mechanism of detecting the β-thalassemia gene by the **1**-based GS: (a) the **1**-PEDOT film modified GCE (**1**-PEDOT/GCE); (b) Au deposited **1**-PEDOT/GCE (Au/**1**-PEDOT/GCE); (c) pDNA grafted Au/**1**-PEDOT/GCE (pDNA/Au/**1**-PEDOT/GCE); (d) BSA-treated pDNA/Au/**1**-PEDOT/GCE (**1**-based GS); (e) **1**-based GS capturing tDNA (dhDNA/Au/**1**-PEDOT/GCE); (f) DPV response of dhDNA/Au/**1**-PEDOT/GCE.

as dhDNA/Au/**1**-PEDOT/GCE, Scheme 2e) based on the principle of complementary base pairing. At this point, the electrochemical signals will be markedly changed after detecting tDNA, giving out the obviously decreased DPV signal (Scheme 2f).

The DPV response can be explained as follows. As we all know, because of the contained negatively-charged phosphate residues, the whole DNA chain is negative. For dhDNA/Au/**1**-PEDOT/GCE, the dhDNA formed by the hybridization of pDNA and tDNA will possess more negative charges than single pDNA strands, leading to larger electrostatic repulsion between negatively charged electrode surfaces and $[Fe(CN)_6]^{3-/4-}$ ions. That is to say, the dhDNA chain formed by the hybridization of pDNA and tDNA may work as an "electronic shield layer", which will largely hinder interfacial electron transfer on the electrode surface.[51,52] In contrast, the electrostatic repulsion between $[Fe(CN)_6]^{3-/4-}$ and single strand pDNA is relatively weaker. Consequently, once tDNA is detected, the dhDNA/Au/**1**-PEDOT/GCE will show reduced conductivity and decreased DPV signal compared with pDNA/Au/**1**-PEDOT/GCE.

In order to obtain the most reliable results for tDNA detection, some key parameters in the process of constructing GS were optimized with DPV signals being the criterion. First of all, to provide enough active sites for grafting pDNA, the electrochemical deposition time of Au NPs was optimized. As can be seen from Fig. 5 and Fig. S21,† the conductivity of Au/**1**-PEDOT/GCEs gradually increases with electrochemical deposition time changing from 20 s to 80 s, whereas the conductivity begins to decrease with prolonging electrochemical deposition time. As a result, 80 s was chosen as the most suitable electrochemical deposition time of Au NPs. For the characterization of the Au/**1**-PEDOT film, XPS, AFM and SEM-EDS were
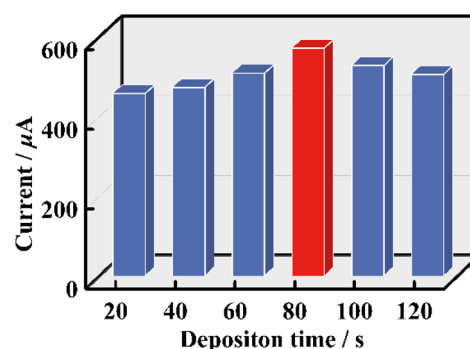


**Fig. 5** DPV signals of Au/**1**-PEDOT/GCEs with different electrodeposition times of Au NPs in Fe-PBS solution (pH = 7.4).

conducted. In addition to the contained elements in the **1**-PEDOT film, two more characteristic peaks belonging to Au (Au 4f5/2: 84.8 eV, Au 4f7/2: 88.5 eV) are observed in the XPS spectrum of the Au/**1**-PEDOT film,[53] testifying the deposition of Au NPs in the **1**-PEDOT film (Fig. S22†). Moreover, both AFM and SEM images indicate the flatness as well as the integrity of the **1**-PEDOT film after Au deposition (Fig. S23 and S24†), while the SEM-EDS elemental mapping images further confirm the homogeneous distribution of Au NPs on the film (Fig. S24†).

Secondly, to ensure the grafting of pDNA on Au sites, the pDNA incubation time and the concentration of pDNA were optimized. As shown in Fig. 6, when the same concentration of pDNA ($1 \times 10^{-8}$ mol L$^{-1}$) is applied for the grafting of pDNA on Au/**1**-PEDOT/GCE, the read out DPV signals increases obviously when the incubation time is less than 2 h.
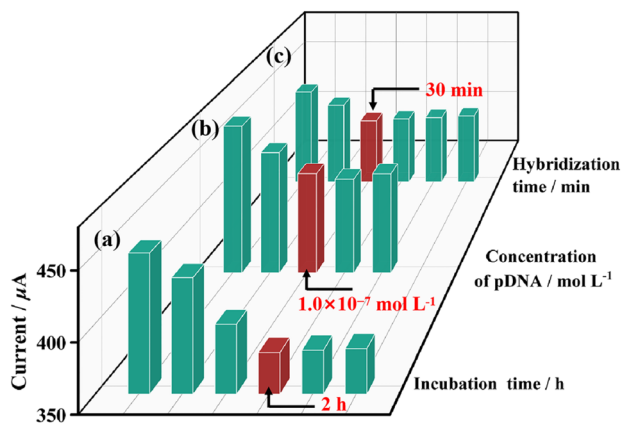
**Fig. 6** (a and b) DPV signal variation of Au/**1**-PEDOT/GCE with different pDNA incubation time and different pDNA concentration. (c) DPV signal variation of dhDNA/Au/**1**-PEDOT/GCE with different hybridization time. [DPV curves were measured in Fe-PBS (pH = 7.4)].

Whereafter, the DPV signal intensity remains stable, which manifests that the incubation reaction is accomplished in 2 h (Fig. S25†). So, a period of 2 h was chosen as the best pDNA incubation time. Then, DPV signals of pDNA/Au/**1**-PEDOT/ GCEs with different pDNA concentrations were measured. It can be seen that the intensity of DPV peaks reduces when the concentration of pDNA ranges from $1 \times 10^{-9}$ mol L$^{-1}$ to $1 \times 10^{-7}$ mol L$^{-1}$, and then keeps almost unchanged on increasing the pDNA concentration (Fig. 6 and Fig. S26†). Accordingly, the optimized conditions for the graft pDNA were 2 h and $1 \times 10^{-7}$ mol L$^{-1}$ pDNA solution. To evaluate the best reaction time for the hybridization of pDNA and tDNA, 10 μL tDNA solution ($5 \times 10^{-10}$ mol L$^{-1}$) was applied on the pDNA/Au/**1**-PEDOT/GCE surface, and the obtained dhDNA/Au/**1**-PEDOT/ GCEs with different hybridization times (10–60 min) were tested by DPV. According to the experimental results, the current signal response shows a decreasing tendency at first and then reaches a stable platform after 30 min, indicating that the hybridization process is basically completed in 30 min (Fig. 6 and S27†). Therefore, 30 min was supposed to be sufficient for the hybridization procedure.

To verify the successful modification of the working electrode in each step during the process of the **1**-based GS construction, the CV method was employed to examine the variation of the electrical conductivity of the working electrode in each step. As shown in Fig. S28,† all the modified GCEs exhibit enhanced peak currents and electroactive areas compared with the bare GCE, demonstrating that the electrical conductivities of the modified electrodes increase. Moreover, the electrical conductivity of Au/**1**-PEDOT/GCE is much higher than that of **1**-PEDOT/GCE owing to the electrochemical deposition of Au on the electrode surface. After the electronegative pDNA is fixed on the surface of Au/**1**-PEDOT/GCE, the peak current and electroactive area of pDNA/Au/**1**-PEDOT/GCE decrease. Finally, the formation of double helix DNA by combining tDNA with pDNA leads to a further decrease of the peak current and electroactive area.

Under these optimal conditions, the sensibility of the **1**-based GS platform (pDNA/Au/**1**-PEDOT/GCE) detecting tDNA was evaluated using DPV and EIS techniques. As can be seen from Fig. 7a and b, the read-out DPV signal of the GS detecting tDNA goes down linearly with the concentration of tDNA ranging from $1 \times 10^{-12}$ mol L$^{-1}$ to $5 \times 10^{-9}$ mol L$^{-1}$. This is because more tDNA strands in the solution result in more dhDNA ("electron shield layer") on the surface of the GS, which hinders the conduction of electrons to some extent. Moreover, within this concentration range, the current intensity ($I$) has a linear relationship with the logarithm of the tDNA concentration, and the regression equation is $I = -26.67 \lg c + 82.91$ with a correlation coefficient ($R^2$) of 0.9866. On this basis, the limit of detection (LOD) for tDNA identification was $2.6 \times 10^{-13}$ mol L$^{-1}$ (Fig. 7c). Excitingly, compared with some previously reported sensors for the β-thalassemia gene, the **1**-based GS has a relatively wider linear range and a lower LOD (Table S2†).

Beyond that, repeatability, selectivity and anti-interference ability are also important criteria for evaluating whether a newly-developed GS is qualified. For this purpose, five pDNA/ Au/**1**-PEDOT/GCEs were prepared under the same conditions to detect $5 \times 10^{-11}$ mol L$^{-1}$ tDNA. As no significant changes in DPV signals (the relative standard deviation was about 2.9%) can be observed, it proves the outstanding repeatability of



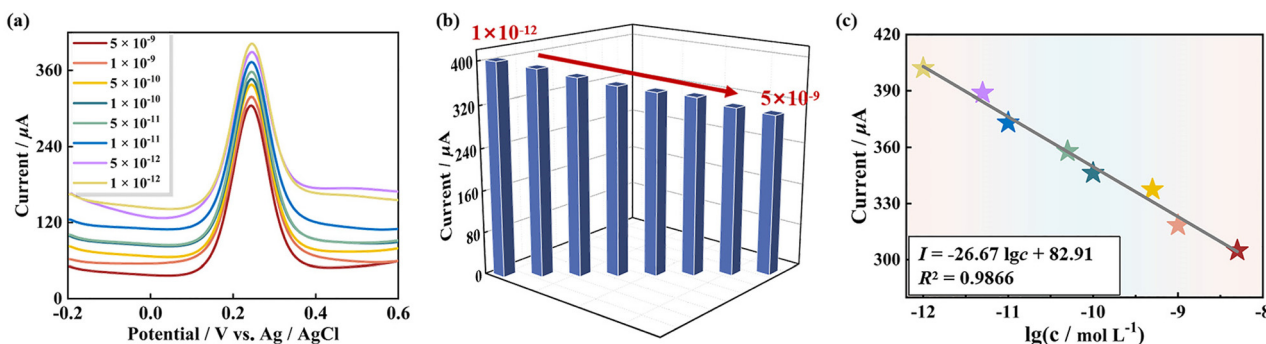**Fig. 7** (a and b) DPV curves and signal intensity of pDNA/Au/**1**-PEDOT/GCEs capturing tDNA with different concentrations. (c) The linear relationship between the DPV signal frontiesy and lgc(tDNA). All signals were measured in solution Fe-PBS (pH = 7.4).

such a **1**-based GS (Fig. S29†). Additionally, according to the principle of complementary base pairing, the specific binding of pDNA and tDNA should be irreplaceable. To test the specificity of this GS, tDNA, and DNA with non-complementary sequences (ncsDNA: 5′-AATCTCATGGCCGATTCG TT-3′), double-base mismatched DNA (dbmDNA: 5′-CGATTGA-CTCATCCT GAAGT-3′) and three-base mismatched DNA (tbmDNA: 5′-CGATTGACA CATCCTGAAGT-3′) were respectively dropped on the surface of pDNA/Au/**1**-PEDOT/GCEs (the concentrations of all the DNAs were $5 \times 10^{-11}$ mol $L^{-1}$). Apparently, only the **1**-based GS capturing tDNA (dhDNA/Au/**1**-PEDOT/GCE) exhibits a significant decrease of the peak current, while none of the other DNA chains (ncsDNA, dbmDNA or tbmDNA) can be identified by the **1**-based GS (Fig. S30†). This is because the hybridization process occurs between completely complementary tDNA and pDNA. In addition, the anti-interference ability of this GS was evaluated by detecting tDNA accompanied by one or several interferents (ncsDNA, dbmDNA and tbmDNA). It can be observed that the existence of interferents hardly influences the DPV response for tDNA, demonstrating a favorable anti-interference ability (Fig. S31†). The above-mentioned results confirm the great potential of **1**-based GS in future applications.

## Conclusions

In conclusion, an innovative $P^V$–$Sb^{III}$ double-HA intercalatated poly(POT) **1** was synthesized using ethylenediamine tetramethylphosphoric acid with potential HA sites and functional organic groups. Intriguingly, the organic–inorganic hybrid Dawson-like $\{C_6N_2P_4SbW_{15}\}$ building block is present in the architecture of **1**, which is quite different from the previously-reported either the $\{(XW_6)(XW_9)\}$ containing single-HA or the emerging dual-HA inserted $\{(XW_6)(X'W_9)\}$. Whereafter, a **1**-PEDOT film with prominent conductivity was prepared by the electropolymerization method, which exhibits great potential in electrochemical applications. Furthermore, a thalassemia GS was fabricated using **1**-PEDOT modified GCE as the working electrode, producing a sensitive DPV response. It shows a low detection limit and wide response range, providing a feasible strategy for trace detection of the β-thalassemia gene. As we know, such a poly(POT)-based thalassemia GS is the first example of a poly(POT)-based thalassemia electrochemical sensor. Applying elemento-organic compounds as dual-functional ligands in this work provides a new idea for building more giant and innovative poly(POT) nanoclusters. Meanwhile, the performance exploration for **1** being used in constructing β-thalassemia GS in some degree promotes the integration of chemistry and biology.

## Author contributions

Wenshu Zhang and Dan Wang performed syntheses, characterization, electrochemical properties and wrote the manuscript. Zixu Wang and Mengya Cao participated in PXRD, IR and TG studies. Lijuan Chen and Junwei Zhao provided research ideas, determined crystal structures and revised all over the manuscript.

## Conflicts of interest

There are no conflicts to declare.

## Acknowledgements

## References

1 L. F. Lian, H. Y. Zhang, S. An, W. Chen and Y.-F. Song, Polyoxometalates-based heterogeneous catalysts in acid catalysis, *Sci. China: Chem.*, 2021, **64**, 1117–1130.

2 L. B. Ni, G. Yang, Y. Liu, Z. Wu, Z. Y. Ma, C. Shen, Z. X. Lv, Q. Wang, X. X. Gong, J. Xie, G. W. Diao and Y. G. Wei, Self-assembled polyoxometalate nanodots as bidirectional cluster catalysts for polysulfide/sulfide redox conversion in lithium–sulfur batteries, *ACS Nano*, 2021, **15**, 12222–12236.

3 L. Fu, H. Q. Gao, M. Yan, S. Z. Li, X. Y. Li, Z. F. Dai and S. Q. Liu, Polyoxometalate-based organic–inorganic hybrids as antitumor drugs, *Small*, 2015, **11**, 2938–2945.

4 H. L. Li, C. Lian, L. J. Chen, J. W. Zhao and G.-Y. Yang, Two unusual nanosized $Nd^{3+}$-substituted selenotungstate aggregates simultaneously comprising lacunary Keggin and Dawson polyoxotungstate segments, *Nanoscale*, 2020, **12**, 16091–16101.

5 T. Minato, K. Suzuki, K. Yamaguchi and N. Mizuno, Synthesis and disassembly/reassembly of giant ring-shaped polyoxotungstate oligomers, *Angew. Chem., Int. Ed.*, 2016, **55**, 9630–9633.

6 J.-C. Liu, J.-F. Wang, Q. Han, P. Shangguan, L.-L. Liu, L.-J. Chen, J.-W. Zhao, C. Streb and Y.-F. Song, Multi-component self-assembly of a giant heterometallic polyoxotungstate supercluster with antitumor activity, *Angew. Chem., Int. Ed.*, 2021, **60**, 11153–11157.

7 S.-R. Li, H.-Y. Wang, H.-F. Su, H.-J. Chen, M.-H. Du, L.-S. Long, X.-J. Kong and L.-S. Zheng, A giant 3d-4f polyoxometalate super-tetrahedron with high proton conductivity, *Small Methods*, 2021, **5**, 2000777.

**610** | *Inorg. Chem. Front.*, 2024, **11**, 602–612

This journal is © the Partner Organisations 2024

8  J. Jiang, Y. Z. Li, L. L. Liu, L. J. Chen, J. W. Zhao, C. Streb and Y.-F. Song, First ultrathin pure polyoxometalate 2D material as a peroxidasemimicking aatalyst for detecting oxidative stress biomarkers, *ACS Appl. Mater. Interfaces*, 2023, **15**, 1486–1494.

9  S. G. Mitchell, C. Streb, H. N. Miras, T. Boyd, D.-L. Long and L. Cronin, Face-directed self-assembly of an electronically active Archimedean polyoxometalate architecture, *Nat. Chem.*, 2010, **2**, 308–312.

10  X. Xu, R. R. Meng, C. T. Lu, L. Meng, L. J. Chen and J. W. Zhao, Acetate-decorated tri-Ln(III)-containing antimonotungstates with a tetrahedral $\{WO_4\}$ group as a structure-directing template and their luminescence properties, *Inorg. Chem.*, 2020, **59**, 3954–3963.

11  M. Ibrahim, V. Mereacre, N. Leblanc, W. Wernsdorfer, C. E. Anson and A. K. Powell, Selbstorganisation eines riesigen tetraedrischen 3d-4f-einzelmolekül-magneten innerhalbeines polyoxometallatsystems, *Angew. Chem.*, 2015, **127**, 15795–15799.

12  K. Yonesato, H. Ito, H. Itakura, D. Yokogawa, T. Kikuchi, N. Mizuno, K. Yamaguchi and K. Suzuki, Controlled assembly synthesis of atomically precise ultrastable silver nanoclusters with polyoxometalates, *J. Am. Chem. Soc.*, 2019, **141**, 19550–19554.

13  Q. Han, Z. Li, X. M. Liang, Y. Ding and S.-T. Zheng, Synthesis of a 6 nm-long transition-metal–rare-earth-containing polyoxometalate, *Inorg. Chem.*, 2019, **58**, 12534–12537.

14  U. Kortz, F. Hussain and M. Reicke, The ball-shaped heteropolytungstates $[\{Sn(CH_3)_2(H_2O)\}_{24}\{Sn(CH_3)_2\}_{12}(A\text{-}XW_9O_{34})_{12}]^{36-}$, *Angew. Chem., Int. Ed.*, 2005, **44**, 3773–3777.

15  X. D. Jia, J. Jiang, L. L. Liu, L. N. Meng, L. J. Chen and J. W. Zhao, Two innovative fumaric acid bridging lanthanide-encapsulated hexameric selenotungstates containing mixed building units and electrochemical performance for detecting mycotoxin, *Inorg. Chem.*, 2022, **61**, 10965–10976.

16  S. S. Xie, J. Jiang, D. Wang, Z. G. Tang, R. F. Mi, L. J. Chen and J. W. Zhao, Tricarboxylic-ligand-decorated lanthanoid-inserted heteropolyoxometalates built by mixed-heteroatom-directing polyoxotungstate units: syntheses, structures, and electrochemical sensing for 17β-Estradiol, *Inorg. Chem.*, 2020, **60**, 7536–7544.

17  X.-X. Li, D. Zhao and S.-T. Zheng, Recent advances in POM-organic frameworks and POM-organic polyhedra, *Coord. Chem. Rev.*, 2019, **397**, 220–240.

18  M.-H. Du, X.-Y. Zheng, X.-J. Kong, L.-S. Long and L.-S. Zheng, Synthetic protocol for assembling giant heterometallic hydroxide clusters from building blocks: rational design and efficient synthesis, *Matter*, 2020, **3**, 1334–1349.

19  Q. Zheng, L. Vilà-Nadal, Z. L. Lang, J.-J. Chen, D.-L. Long, J. S. Mathieson, J. M. Poblet and L. Cronin, Self-sorting of heteroanions in the assembly of cross-shaped polyoxometalate clusters, *J. Am. Chem. Soc.*, 2018, **140**, 2595–2601.

20  J. Yan, D.-L. Long and L. Cronin, Development of a building block strategy to access gigantic nanoscale heteropolyoxo-tungenesensortates by using $SeO_3^{2-}$ as a template linker, *Angew. Chem., Int. Ed.*, 2010, **49**, 4117–4120.

21  S. S. Xie, D. Wang, Z. X. Wang, J. C. Liu, L. J. Chen and J. W. Zhao, Dual-heteroatom-templated lanthanoid-inserted heteropolyoxo-tungstates simultaneously comprising Dawson and Keggin subunits and their composite film applied for electrochemical immunosensing of auximone, *Inorg. Chem. Front.*, 2022, **9**, 350–362.

22  L. L. Liu, J. Jiang, X. Y. Liu, G. P. Liu, D. Wang, L. J. Chen and J. W. Zhao, First series of mixed ($P^{III}$, $Se^{IV}$)-heteroatoms oriented rare-earth embedded polyoxotungstates containing distinct building blocks, *Inorg. Chem. Front.*, 2020, **7**, 4640–4651.

23  T. T. Gong, J. Jiang, S. Yang, J. C. Liu, L. J. Chen and J. W. Zhao, Lanthanide-incorporated polyoxometalates assembled from mixed-heteroatom-oriented three-layered cage clusters, *Inorg. Chem.*, 2022, **61**, 18147–18153.

24  Q. Chang, X. Y. Meng, W. J. Ruan, Y. W. Feng, R. Li, J. Y. Zhu, Y. Ding, H. J. Lv, W. Wang, G. Y. Chen and X. K. Fang, Metal−organic cages with $\{SiW_9Ni_4\}$ polyoxotungstate nodes, *Angew. Chem., Int. Ed.*, 2022, **61**, e202117637.

25  Z. W. Liu, W. Wang, J. K. Tang, W. Q. Li, W. Y. Yin and X. K. Fang, Chain length effect in the functionalization of polyoxometalates with α, ω-alkyldiphosphonates, *Chem. Commun.*, 2019, **55**, 6547–6550.

26  G. Sazani, M. H. Dickman and M. T. Pope, Organotin derivatives of α-$[X^{III}W_9O_{33}]^{9-}$ (X = As, Sb) heteropolytungstates. Solution- and solid-state characterization of $[\{(C_6H_5Sn)_2O\}_2H(\alpha\text{-}AsW_9O_{33})_2]^{9-}$ and $[(C_6H_5Sn)_3Na_3(\alpha\text{-}SbW_9O_{33})_2]^{6-}$, *Inorg. Chem.*, 2000, **39**, 939–943.

27  S. J. Li, Y. F. Zhou, N. N. Ma, J. Zhang, Z. P. Zheng, C. Streb and X. N. Chen, Organoboron-functionalization enables the hierarchical assembly of giant polyoxometalate nanocapsules, *Angew. Chem., Int. Ed.*, 2020, **59**, 8537–8540.

28  Y. Huo, Z. Y. Huo, P. T. Ma, J. P. Wang and J. Y. Niu, Polyoxotungstate incorporating organotriphosphonate ligands: synthesis, characterization, and catalytic for alkene epoxidation, *Inorg. Chem.*, 2015, **54**, 406–408.

29  D. Wang, Y. M. Li, Y. Zhang, X. Xu, Y. Liu, L. J. Chen and J. W. Zhao, Construction of $Ln^{3+}$-substituted arsenotungstates modified by 2,5-thiophenedicarboxylic acid and application in selective fluorescence detection of $Ba^{2+}$ in aqueous solution, *Inorg. Chem.*, 2020, **59**, 6839–6848.

30  D. Wang, J. Jiang, M.-Y. Cao, S.-S. Xie, Y.-M. Li, L.-J. Chen, J.-W. Zhao and G.-Y. Yang, An unprecedented dumbbell-shaped pentadeca-nuclear W−Er heterometal cluster stabilizing nanoscale hexameric arsenotungstate aggregate and electrochemical sensing properties of its conductive hybrid film-modified electrode, *Nano Res.*, 2022, **15**, 3628–3637.

31  J. Li, N. Z. Song, M. L. Wang, Z. M. Zhang, Y. Z. Li, L. J. Chen and J. W. Zhao, Two types of subgroup-valence heteroatoms ($P^{III}$, $Te^{IV}$) synergistically controlling octa-$Ce^{III}$-encapsulated heteropolyoxo-tungstate and its electro-

This journal is © the Partner Organisations 2024

*Inorg. Chem. Front.*, 2024, **11**, 602–612 | **611**

chemical Recognition properties, *Inorg. Chem.*, 2022, **61**, 17166–17177.

32 F. Tang, Y. Z. Li, B. X. Zeng, G. P. Liu, J. W. Zhao and L. J. Chen, Lamellar nanocomposite based on a 1D cray-fish-like ceIIIsubstituted phospho(III)tungstate semi-conductor and polyaniline used as a high-performance humidity sensing device, *ACS Appl. Mater. Interfaces*, 2022, **14**, 48876–48887.

33 H. K. Guo, M. H. Zeng, X. Li, H. B. He, L. X. Wu and H. L. Li, Multifunctional enhancement of proton-conduc-tive, stretchable, and adhesive performance in hybrid polymer electrolytes by polyoxometalate nanoclusters, *ACS Appl. Mater. Interfaces*, 2021, **13**, 30039–30050.

34 H. K. Guo, L. B. Li, X. L. Xu, M. H. Zeng, S. C. Chai, L. X. Wu and H. L. Li, Semi-solid superprotonic supramole-cular polymer electrolytes based on deep eutectic solvents and polyoxometalates, *Angew. Chem., Int. Ed.*, 2022, **61**, e202210695.

35 H. Liu, J. Zhang, X. X. Xu and Q. Wang, A polyoxometalate-based binder-free capacitive deionization electrode for highly efficient sea water desalination, *Chem. – Eur. J.*, 2020, **26**, 4403–4409.

36 I. Sakthinathan, J. Köhling, V. Wagner and T. McCormac, Layer-by-layer construction of a nanoarchitecture by polyox-ometalates and polymers: enhanced electrochemical hydro-gen evolution reaction, *ACS Appl. Mater. Interfaces*, 2023, **15**, 2861–2872.

37 D. Wang, L. L. Liu, J. Jiang, L. J. Chen and J. W. Zhao, Polyoxometalate-based composite materials in electro-chemistry: state-of-the-art progress and future outlook, *Nanoscale*, 2020, **12**, 5705–5718.

38 T. C. Jiang, P. B. Wan, Z. J. Ren and S. K. Yan, Anisotropic polyaniline/SWCNT composite films prepared by in situ electropolymerization on highly oriented polyethylene for high-efficiency ammonia sensor, *ACS Appl. Mater. Interfaces*, 2019, **11**, 38169–38176.

39 F. X. Jiang, R. R. Yue, Y. H. Du, J. K. Xu and P. Yang, A one-pot 'green' synthesis of Pd-decorated PEDOT nanospheres for nonenzymatic hydrogen peroxide sensing, *Biosens. Bioelectron.*, 2013, **44**, 127–131.

40 W. L. Zhang, R. Jamal, R. Y. Zhang, Z. N. Yu, Y. Q. Yan, Y. C. Liu, Y. Ge and T. Abdiryim, Self-assembly of pendant functional groups grafted PEDOT as paracetamol detection material, *Phys. Chem. Chem. Phys.*, 2020, **22**, 3592–3603.

41 Y. L. He, J. H. Li, K. Lou, L. F. Li, J. B. Chen and J. Y. Li, Engineering reduced graphene oxide aerogel produced by effective γ-ray radiation-induced self-assembly and its application for continuous oil–water separation, *Ind. Eng. Chem. Res.*, 2016, **55**, 3775–3781.

42 I. Ivanko, J. Svoboda, M. Lukešová, I. Šeděnkov and E. Tomšík, Hydrogen bonding as a tool to control chain structure of PEDOT: electrochemical synthesis in the pres-ence of different electrolytes, *Macromolecules*, 2020, **53**, 2464–2473.

43 A. U. Alam, Y. H. Qin, M. Catalano, L. H. Wang, M. J. Kim, M. M. R. Howlader, N.-X. Hu and M. J. Deen, Tailoring MWCNTs and β-cyclodextrin for sensitive detection of acet-aminophen and estrogen, *ACS Appl. Mater. Interfaces*, 2018, **10**, 21411–21427.

44 M. X. Li, Y. Zhu, N. Song, C. Wang and X. F. Lu, Fabrication of Pt nanoparticles on nitrogen-doped carbon/Ni nano-fibers for improved hydrogen evolution activity, *J. Colloid Interface Sci.*, 2018, **514**, 199–207.

45 Q. He, Y. Y. Wan, H. L. Jiang, Z. W. Pan, C. Q. Wu, M. Wang, X. J. Wu, B. J. Ye, P. M. Ajayan and L. Song, Nickel vacancies boost reconstruction in nickel hydroxide electrocatalyst, *ACS Energy Lett.*, 2018, **3**, 1373–1380.

46 M. H. Hodroj, R. Bou-Fakhredin, W. Nour-Eldine, H. A. Noureldine, M. H. A. Noureldine and A. T. Taher, Thalassemia and malignancy: an emerging concern, *Blood Rev.*, 2019, **37**, 100585.

47 E. Hamidi-Asl, J. B. Raoof, N. Naghizadeh, H. Akhavan-Niaki, R. Ojani and A. Banihashemi, A bimetallic nano-composite modified genosensor for recognition and determination of thalassemia gene, *Int. J. Biol. Macromol.*, 2016, **91**, 400–408.

48 M.-B. Gholivand and A. Akbari, A sensitive electrochemical genosensor for highly specific detection of thalassemia gene, *Biosens. Bioelectron.*, 2019, **129**, 182–188.

49 S. Devanesan, F. AlQahtani, M. S. AlSalhi, K. Jeyaprakash and V. Masilamani, Diagnosis of thalassemia using fluo-rescence spectroscopy, auto-analyzer, and hemoglobin electrophoresis—A prospective study, *J. Infect. Public Health*, 2019, **12**, 585–590.

50 G. Breveglieri, E. D'Aversa, T. E. Gallo, P. Pellegatti, G. Guerra, L. C. Cosenza, A. Finotti, R. Gambari and M. Borgatti, A novel and efficient protocol for surface plasmon resonance based detection of four β-thalassemia point mutations in blood samples and salivary swabs, *Sens. Actuators, B*, 2018, **260**, 710–718.

51 F. Jia, D. Liu, N. Dong, Y. Y. Li, S. Y. Meng and T. Y. You, Interaction between the functionalized probes: The depressed efficiency of dual-amplification strategy on ratio-metric electrochemical aptasensor for aflatoxin B1, *Biosens. Bioelectron.*, 2021, **182**, 113169.

52 S. S. Mahshid, S. Camiré, F. Ricci and A. Vallée-Bélisle, A highly selective electrochemical DNA-based sensor that employs steric hindrance effects to detect proteins directly in whole blood, *J. Am. Chem. Soc.*, 2015, **137**, 15596–15599.

53 L.-C. Wang, Y.-M. Liu, M. Chen, Y. Cao, H.-Y. He and K.-N. Fan, MnO2 nanorod supported gold nanoparticles with enhanced activity for solvent-free aerobic alcohol oxi-dation, *J. Phys. Chem. C*, 2008, **112**, 6981–6987.

**612** | *Inorg. Chem. Front.*, 2024, **11**, 602–612

This journal is © the Partner Organisations 2024